Biophysical Reports

ARTICLE

Fine-tuning of FeS proteins monitored via pulsed EPR redox potentiometry at Q-band

Melanie Heghmanns,[1] Alexander Günzel,[2] Dörte Brandis,[1] Yury Kutin,[1] Vera Engelbrecht,[2] Martin Winkler,[2] Thomas Happe,[2,*] and Müge Kasanmascheff[1,*]

[1]TU Dortmund University, Department of Chemistry and Chemical Biology, Dortmund, Germany and [2]Ruhr University Bochum, Faculty of Biology and Biotechnology, Photobiotechnology, Bochum, Germany

ABSTRACT As essential electron translocating proteins in photosynthetic organisms, multiple plant-type ferredoxin (Fdx) isoforms are involved in a high number of reductive metabolic processes in the chloroplast. To allow quick cellular responses under changing environmental conditions, different plant-type Fdxs in *Chlamydomonas reinhardtii* were suggested to have adapted their midpoint potentials to a wide range of interaction partners. We performed pulsed electron paramagnetic resonance (EPR) monitored redox potentiometry at Q-band on three Fdx isoforms for a straightforward determination of their midpoint potentials. Additionally, site-directed mutagenesis was used to tune the midpoint potential of *Cr*Fdx1 in a range of approximately −338 to −511 mV, confirming the importance of single positions in the protein environment surrounding the [2Fe2S] cluster. Our results present a new target for future studies aiming to modify the catalytic activity of *Cr*Fdx1 that plays an essential role either as electron acceptor of photosystem I or as electron donor to hydrogenases under certain conditions. Additionally, the precisely determined redox potentials in this work using pulsed EPR demonstrate an alternative method that provides additional advantages compared with the well-established continuous wave EPR technique.

WHY IT MATTERS In this work, we determined midpoint potentials of distinct ferredoxin isoforms found in *Chlamydomonas reinhardtii* using pulsed electron paramagnetic resonance spectroscopy at Q-band. Site-directed mutagenesis was used to tune the midpoint potential of ferredoxin 1, known as PetF, in a range of −338 to −511 mV. Our results serve as a basis to design new experiments for unraveling the distinct functions of ferredoxin isoforms and illuminate the decisive role of individual positions in the secondary ligand sphere of the cofactor in tuning the midpoint potential of redox proteins.

INTRODUCTION

Proteins containing iron-sulfur (FeS) clusters are one of the major electron transfer protein classes in biology (1–3). The midpoint potential (E_m) difference between an FeS protein and its partner determines the kinetics and efficiency of electron transfer reactions (4,5). The redox range of FeS proteins is wide and mostly dictated by the protein environment in the immediate vicinity of the bound FeS cluster (6–9). Developing methods for precise measurements of E_m and determining factors that affect its magnitude are therefore important first steps toward understanding structure-function relationships that control electron transfer processes in both native and rationally designed proteins.

Primary ligands play a major role in the coarse adjustment of the E_m range of FeS clusters. Long-range protein effects and interactions of the metal cluster with the secondary coordination sphere fine-tune the E_m values and thus electron transfer processes (8,10). Multiple types of interactions have been shown to drastically influence the potentials of metal centers in protein environments, including hydrogen bonding interactions, hydrophobicity and solvent exposure, aromatic interactions, and net charge effects (10–12).

Ferredoxins (Fdxs) are ubiquitous FeS proteins that function as electron acceptors and donors in diverse metabolic pathways. Interestingly, the evolution of more complex FeS proteins is discussed to have started

Submitted May 20, 2021, and accepted for publication August 30, 2021.

*Correspondence: thomas.happe@rub.de or muege.kasanmascheff@tu-dortmund.de

Melanie Heghmanns and Alexander Günzel contributed equally to this work.

Editor: Paul Schanda.

https://doi.org/10.1016/j.bpr.2021.100016

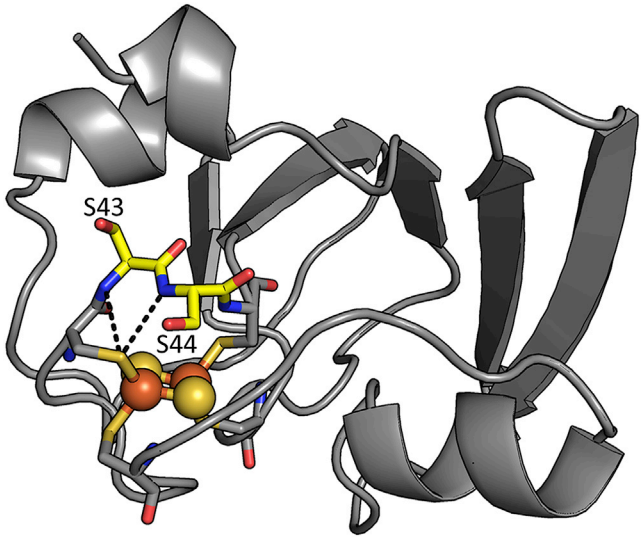

FIGURE 1 Cartoon structure of *Cr*Fdx1 (Protein Data Bank, PDB: 6lk1). [2Fe2S] cluster with ligating cysteines shown as a ball and stick model. Serine 43 and serine 44 are shown as yellow sticks. Potential hydrogen bonds from amide nitrogen atoms (*blue*) to sulfur atoms (*dark yellow*) of the ligating cysteine are shown with black dashed lines.

from ancient Fdxs, which were incorporated into larger electron transfer chains or adapted toward metallocofactors of higher complexity (13). Plant-type Fdxs, which are mainly found in the chloroplasts of photosynthetic algae, cyanobacteria, and higher plants (14), are characterized by their relatively low midpoint potentials ranging from −230 to −420 mV (15). Their [2Fe2S] cluster in its oxidized state has usually two high-spin Fe^{3+} ions ($S = 5/2$) antiferromagnetically coupled, yielding a total spin $S_T = 0$ in the ground state. Upon reduction of one Fe^{3+} ion to high-spin Fe^{2+} ($S = 2$), the ground state has a total spin $S_T = 1/2$, producing a paramagnetic species with a localized electronic structure that can be identified and characterized via electron paramagnetic resonance (EPR) spectroscopy (16,17). As small (∼10 kDa) and soluble metalloproteins having the same fold and FeS cluster binding motif (3), the versatile plant-type Fdxs are effective models for assessing the influence of the protein surroundings on FeS clusters.

The unicellular green alga *Chlamydomonas reinhardtii* (Cr) is known to provide an unusual wealth of 12 different Fdx isoforms (*Cr*Fdx1–12) (18,19). All genes encode for plant-type Fdxs with characteristic [2Fe2S] clusters and a conserved binding motif (Fig. 1) (20). Thus far, only some of the *Cr*Fdx isoforms were assigned to specific functions and interaction partners under certain environmental conditions. The most abundant isoform *Cr*Fdx1, also known as PetF, plays an essential role as an electron acceptor of photosystem I (21,22). Under anaerobiosis and nutrient deprivation, *Cr*Fdx1 becomes the electron donor to the hydrogenase HydA1, which catalyzes the reversible reduction of H^+ to H_2 (23). Furthermore, *Cr*Fdx2–5 are suggested to be involved in nitrite reduction, nitrogen assimilation, glycolysis, and hydrogenase maturation, respectively (24–26). E_m values of *Cr*Fdx1 (−410 mV (22)) and *Cr*Fdx2 (−331 mV (26)), which have been determined previously by distinct methods, such as cyclic voltammetry, ultraviolet-visible spectroscopy (UV/Vis), and continuous wave (cw) EPR-monitored redox titrations, differ substantially (22,25,26). By comparing the sequences and structures of these Fdxs, Boehm et al. (26) were able to shift the E_m of *Cr*Fdx2 closer to that of *Cr*Fdx1 by exchanging a single amino acid. The same mutation also led to shifts in detected *g*-values, indicating the role of this residue in fine-tuning the electronic properties of the [2Fe2S] cluster residing in *Cr*Fdx2. Yet electrochemical data on the other isoforms is scarce.

Cyclic voltammetry, UV/Vis, and EPR-monitored redox potentiometry are established and highly effective methods for the determination of E_ms of Fdxs (11,27–29). EPR spectroscopy serves to monitor the spectral changes during oxidation-reduction reactions that are driven by the mediated application of defined potentials on redox proteins with at least one paramagnetic state (30). Additionally, it provides structural insights into the protein under study while simultaneously enabling the deconvolution of multiple redox-active species in one protein. In contrast to UV/Vis, EPR-monitored redox potentiometry overcomes the difficulty of separating the contribution from most mediator dyes and is more precise, particularly for Fdxs as they exhibit low extinction coefficients. Moreover, misinterpretations because of background signals or minor impurities can be avoided by comparing the experimental and simulated EPR data.

Herein, we determined the unknown midpoint potential of the isoform *Cr*Fdx3 using pulsed EPR spectroscopy at Q-band (34 GHz). As it was suggested that *Cr*Fdx3 might interact with the [FeFe]-hydrogenases HydA1 and HydA2 from *C. reinhardtii* (24), its redox properties are of high interest. Furthermore, we investigated the effect of substituting specific amino acids surrounding the [2Fe2S] cluster on the midpoint potential of *Cr*Fdx1. This enabled us to identify S43 as a key position to fine-tune the midpoint potential in *Cr*Fdx1 and thus presented a new target for future studies aiming to modify its catalytic activity.

MATERIALS AND METHODS

Protein expression and purification

The *C. reinhardtii* sequences encoding ferredoxins *Cr*Fdx1 (National Center for Biotechnology Information accession number XP_001692808.1), *Cr*Fdx2 (XP_001697912.1), and *Cr*Fdx3 (XP_001691381.1) were amplified from complementary DNA isolated out of total RNA from

culture samples of *C. reinhardtii* strain CC-124. In all cases, known or predicted sequences that may encode transit peptides were omitted. *Cr*Fdx sequences were cloned into vector pASK-IBA7, following a sequence encoding an N-terminal Strep-tagII and a factor Xa cleavage site, according to manufacturer recommendations (IBA Lifesciences, Göttingen, Germany; www.iba-lifesciences.com).

Expression constructs for site-directed mutagenesis variants of *Cr*Fdx1 were generated following the procedure described in the QuikChange-PCR manual from Agilent Technologies (Santa Clara, CA), using the corresponding 5′ overlapping mismatch primer pairs (Table S1).

For the heterologous expression of the different Fdx isoforms and mutagenesis variants, electrocompetent *Escherichia coli* BL21(DE3) ΔiscR cells were transformed using the respective expression construct. 4 L Vogel-Bonner medium was inoculated with overnight grown LB-preculture to an OD_{550} of 0.05 (31). Main cultures were grown at 37°C in a shaking incubator (180 rpm) until an OD_{550} of 0.5 was reached. Gene expression was induced by adding anhydrotetracycline to a final concentration of 0.2 $\mu g \times mL^{-1}$, and expression cultures were kept for 16 h at 20°C in a shaking incubator (180 rpm) until cell harvest. Cells were harvested by centrifugation (20 min, 9000 g, and 4°C), and cell pellets were resuspended in 0.1 M Tris-HCl (pH 8). Cell disruption was carried out by ultrasonication, and the resulting cell lysate was centrifuged at 165,000 g for 1 h at 4°C. The supernatant was filtered using sterile syringe filters (0.2-μm pore size; SARSTEDT, Newton, NC). The recombinant proteins were purified via affinity chromatography using StrepTag Superflow high-capacity gravity flow columns (IBA Lifesciences), according to manufacturer's recommendations, and concentrated using Amicon Ultracel filters with a 10 kDa cutoff (Merck Millipore, Burlington, MA). Protein concentration was determined via UV/Vis spectroscopy (BioPhotometer D30 from Eppendorf, Hamburg, Germany www.eppendorf.com) at 420 nm applying the Beer-Lambert Law and using a molar extinction coefficient of 9.7 $mM^{-1} \cdot cm^{-1}$ (32). Until further use, all proteins were stored at −80°C in 0.1 M Tris-HCl (pH 8). Fdx from *Spinacia oleracea* (*So*Fdx) and the remaining chemicals used for protein expression and purification were purchased from Sigma-Aldrich (St. Louis, MO).

Redox potentiometry

The FeS cluster occupancy of the purified Fdxs was calculated before each experiment by measuring the absorbance at 420 nm via UV/Vis spectroscopy (NanoDrop 1000; Thermo Fisher Scientific, Waltham, MA). Redox titrations were performed in an anaerobic vinyl tent (~20 ppm O_2; Coy Laboratory Products, Grass Lake, MI) equipped with an electrochemical glass cell (scientific glassblowing service; TU Dortmund University, Dortmund, Germany) built according to the description provided by Wright et al. (29). A final concentration of 200 μM cluster-occupied Fdxs in titration buffer (60 mM HEPES, 40 mM potassium phosphate buffer, and 150 mM NaCl (pH 7.5)) and the following redox mediator dyes of methyl viologen (200 μM), benzyl viologen (200 μM), and 100 μM each of neutral red, safranin O, sodium anthraquinone-2-sulfonate, phenosafranin, and 2-hydroxy-1,4-naphthoquinone were added to the cell. The overall volume of solution within the cell was 770 μL. Under constant stirring, the solution potential was altered by microliter additions of either 2 or 20 mM sodium dithionite (NaDT) solution (reductive titration) or potassium ferricyanide solution (oxidative titration). The potential difference was monitored with a potentiostat (PalmSense4; PalmSens, Houten, the Netherlands) connected to a glass-encased platinum wire, functioning as a working electrode (scientific glassblowing service; TU Dortmund University), and an Ag/AgCl microreference electrode with a 6-mm diameter (Redoxme, Norrköping, Sweden) calibrated with Zobell's solution (33) or a commercially available Ag/AgCl electrode. All herein reported potentials, E_h, are in reference to the standard hydrogen electrode. The potential was altered in ~30 mV steps. After stabilization of ~5–10 min at a given potential, 70 μL of the sample solution was transferred to a 2.8 mm EPR tube (quartz glass capillary ilmasil) and immediately flash frozen in liquid nitrogen. Nine samples were usually withdrawn for each potentiometry series. In addition, an external 200 μM standard of the respective protein was prepared and reduced with 10 mM NaDT for comparison of the spin concentrations.

cw EPR spectroscopy

X-band cw EPR measurements were performed at 15 K using a Bruker ELEXSYS E500 spectrometer equipped with a Bruker ER 4116DM resonator (Bruker, Billerica, MA), Oxford Instruments ESR 900 cryostat (Abingdon, UK), and ITC503 temperature controller. The microwave power level used was 0.63 mW, and magnetic field modulation amplitude was 7 G. The spectra were recorded under nonsaturating conditions.

Q-band cw EPR measurements were performed at 15 and 25 K using a Bruker ELEXSYS E580 spectrometer equipped with a home-built Q-band cw EPR intermediate frequency unit, Bruker ER 5106 resonator, Oxford instruments CF 935 cryostat, and ITC503 temperature controller. The microwave power was in the range of 0.02–20 mW, and magnetic field modulation amplitude was 5 G.

Pulsed EPR spectroscopy

Pulsed EPR (electron spin echo-detected EPR) field-sweep experiments, using a two-pulse Hahn spin echo sequence $\pi/2-\tau-\pi-\tau-$echo without phase cycling, were carried out on a Bruker ELEXSYS E580 Q-band EPR spectrometer equipped with an Oxford Instruments CF935 cryostat and Oxford Instruments MercuryiTC temperature controller. The temperature was kept at 15 K with a sufficiently high flow of liquid He. The Bruker ER 5106QT-2 resonator was critically coupled with the inserted sample height spanning the entire length of the cavity. For comparison of signal intensities, all spectra of a respective sample batch were recorded on the same day under optimized, similar conditions concerning the shot repetition time, pulse lengths, microwave power, τ, and acquisition trigger parameters. The $\pi/2$- and π-pulse lengths varied between 8–11 and 16–22 ns, respectively, whereas τ was kept between 600 and 650 ns and the shot repetition time between 300 and 600 ns, depending on the Fdx type. Either one or two scans with 100 shots/point were accumulated, chosen based on the concentration of the reduced Fdx species. The measurement time varied accordingly between 1.3 and 2.5 min/scan. The phase memory time T_m was measured via a two-pulse echo decay experiment using a $\pi/2-\tau-\pi-\tau-$echo sequence. The relaxation curves were fitted with a stretched exponential function using MATLAB (The MathWorks, Natick, MA). The original pulsed EPR spectra are shown in Fig. S3.

Validation of pulsed EPR at Q-band as an accurate method for determining redox potentials

To validate pulsed EPR as a method for determining redox potentials, the midpoint potential of the well-characterized *So*Fdx was investigated. The rhombic EPR spectrum arising from the reduced [2Fe2S] cluster of *So*Fdx was simulated with $g_{1,2,3} = 2.05, 1.96, 1.89$ (Fig. S1; Table S2), which are in great agreement with the literature values (34). Oxidative potentiometric titrations with *So*Fdx were performed via cw and pulsed EPR spectroscopy at X- and Q-band, respectively (Fig. S2). Both X-band cw and pulsed Q-band EPR spectra of the redox titration series suffered from distinct

background impurities (Figs. S1 and S3). Potential-dependent contributions from the mediator mix, as well as from low amounts of free Mn^{2+} present in the buffer, hampered the uniform background subtraction. Therefore, the EPR intensity of the spectral component at $g_3 = 1.89$, which is well separated from the impurity signals, was used to compare the fractions of the reduced species within a series of titration samples (Fig. S1). The fits to the one-electron Nernst equation, which were almost identical for cw and pulsed EPR measurements, resulted in $E_{m,7.5} = -394 \pm 7$ and ± 5 mV, respectively. A plot of the redox potentials against the logarithm of the concentration ratio of oxidized to reduced (log([Ox]/[Red])) Fdx yields the number of electrons transferred, n. Low n values can be an indicator of incomplete equilibration during redox potentiometry. The *So*Fdx data set yields $n = 1.02$ (inset in Fig. S2), which is in excellent agreement with the expected one-electron transfer reaction. For the quantitative pulsed EPR measurements, several points were considered. In general, an overcoupled resonator is used for Q-band pulsed EPR experiments, but we found the spectral intensities were often poorly reproducible. To circumvent this issue, we performed the experiments with a critically coupled resonator to maximize the reproducibility. As a result of the high-quality factor, Q, pulse microwave power took longer to dissipate and thus required a longer interpulse delay, τ. To control for possible changes in the phase memory time T_m and its effect on the electron spin echo signal intensity, echo decay experiments were carried out for each sample in the series. The T_m time was found to be nearly constant under the varying potential E_h, and thus, its influence on the obtained E_m value was negligible (Figs. S4 and S5; Table S3). This may not be the case for other systems, and we note that the T_m relaxation time needs to be taken into account when pulsed EPR is used for spin quantification. The determination of T_m and the subsequent correction of midpoint potentials, however, is a quick and simple procedure, as explained in the discussion of Table S3.

Here, the identical E_m values obtained from the two datasets established that cw EPR at X-band and pulsed EPR at Q-band are equivalent for quantitative analysis.

Spectral analysis

The EPR spectra were baseline corrected using MATLAB. The absorption spectra were pseudomodulated (modulation amplitude of 3 G) and subsequently simulated with *EasySpin* (35) for a straightforward analysis of g-values, where g_1 corresponds to the low-field spectral feature and g_3 to the high-field one. To exclude any background contributions, the simulated pseudomodulated spectra were integrated, if not stated otherwise, over the whole spectral range for the determination of spin concentrations (36). The obtained intensities were then corrected for dilution and compared to the standard sample (of the same Fdx type) showing the highest spectral intensity within the experimental uncertainty. The spin concentration of the standard was set to 100%, whereas the respective potential was chosen to be -0.47 V according to the E_m of NaDT (37). The fractions of the reduced species were plotted against the corresponding potentials E_h. The data were fitted to the Nernst equation:

$$y(x) = \frac{100}{1 + e^{((x-E_m)/Q)}}$$

yielding the midpoint potential E_m (in volts) for a one-electron transfer, with $Q = (RT)/(nF)$ (R, universal gas constant; T, temperature in Kelvin; n, number of electrons transferred; and F, Faraday constant) (38).

A semi-log plot of E_h versus the common logarithm of the concentration ratio of oxidized ([Ox]) to reduced ([Red]) Fdx yielded the E_m from the y-intercept of the line according to:

$$E_h = E_m + 2.3026 \cdot Q \cdot log \frac{[Ox]}{[Red]}$$

The slope, b, was used to calculate the number of electrons transferred, n, with $b = 0.059$ V/n at 25°C (30,38). The error of the Nernst fit is given within 95% confidence interval. It comprises changes in temperature (±0.3 mV), pH (±1.2 mV), and electrode calibration (39). Errors occurring because of protein denaturation and/or evaporation during the redox titration were averaged out by performing two, namely oxidative and reductive, titrations.

RESULTS

EPR characterization and midpoint potentials of *C. reinhardtii* ferredoxin isoforms

To identify and characterize the [2Fe2S] clusters of the ferredoxin isoforms, we recorded pulsed EPR spectra of *Cr*Fdx1-3 at Q-band. The first-derivative line shapes of the recorded EPR spectra are shown in Fig. 2 *A*. Note that Q-band cw experiments failed to detect EPR signals of at least two isoforms (*Cr*Fdx3 EPR data are shown exemplarily in Fig. S6). A similar observation was reported previously for a different system (40).

All spectra indicate a rhombic symmetry with three principal g-values. The g-values were determined via spectral simulations, for which g-strain was used to fit the linewidths (Table S2). The obtained g-values, which varied slightly among the isoforms ($g_1 = 2.048–2.061$, $g_2 = 1.955–1.971$, and $g_3 = 1.879–1.890$), were all in the range for typical [2Fe2S] clusters (17). These differences are attributed to the distinct tetrahedral environment of the ferrous ion (41). Additional physical differences between the *Cr*Fdx isoforms were examined by comparing the width of the g_3 component, rhombicity $\eta = (g_2 - g_3)/(g_1 - g_{iso})$, g_{iso}, and the parameter $\chi = g_2 - g_3$ (Table S2). Wide g_3 peaks and high χ-values indicate enhanced flexibility of the [2Fe2S] cluster (41). η and g_{iso} are correlated with structural changes of the active site and spin localization within the cluster, respectively (41–43). Small deviations of these parameters are expected as the redox-active centers reside in distinct proteins. Their high overall similarity, however, strongly indicates similar spin localization and structural environments of the [2Fe2S] clusters (Table S2).

Next, we determined the E_m values of each Fdx isoform. The Nernst plots obtained by oxidative and reductive redox titrations monitored via pulsed EPR at Q-band are shown in Fig. 2 *B* (see Fig. S3 for details). We note that the determined E_m values of *Cr*Fdx1 ($E_{m,7.5} = -419$ mV) and *Cr*Fdx2 ($E_{m,7.5} = -332$ mV) are in great agreement with the previously reported values (Table S4) (22,25,26). The E_m of *Cr*Fdx3 that is determined here for the first time is

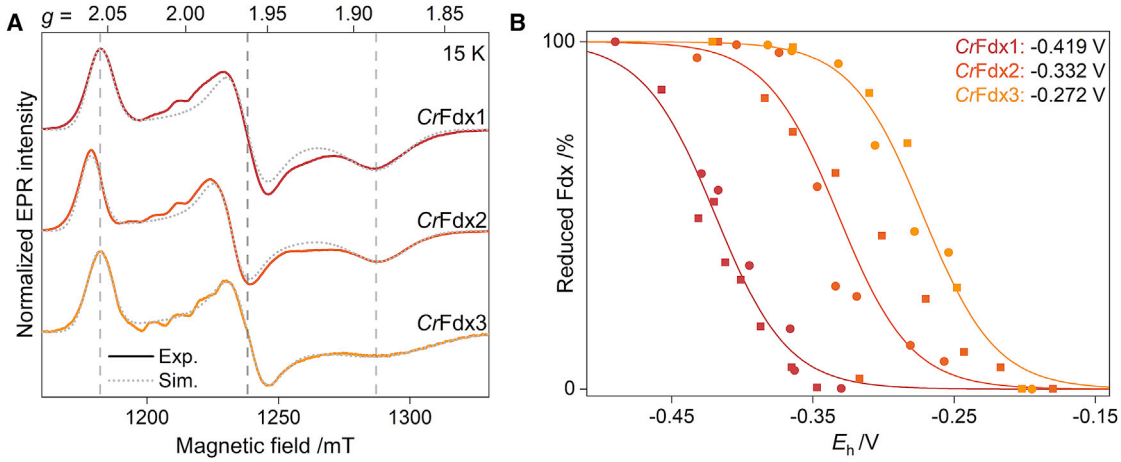

FIGURE 2 (*A*) Comparison of normalized Q-band pseudomodulated pulsed EPR spectra of *Cr*Fdx isoforms. The isoforms were reduced with 10 mM NaDT, and the corresponding simulations are shown with dotted gray lines. The principal *g*-values of *Cr*Fdx1 are marked with vertical dashed lines. Simulation parameters are listed in Table S2. (*B*) Titration curves of the reductive (*circles*) and oxidative (*squares*) redox potentiometry series of the three *Cr*Fdx isoforms monitored via pulsed EPR spectroscopy at Q-band. The reduced Fdx fractions were obtained by double integration of the simulated pseudomodulated pulsed EPR spectra. The data points were fitted to the one-electron Nernst equation yielding the midpoint potential.

−272 mV. Surprisingly, the midpoint potential of this isoform is not only substantially higher than that of *Cr*Fdx1 ($E_{m,7.5} = -419$ mV) but also remarkably high for plant- and cyanobacterial-type Fdxs (25). A comparable $E_{m,7.5} = -243$ mV was recently obtained for the cyanobacterial Fdx2 from *Synechocystis sp.* PCC 6803 (44).

We note that the oxidative and reductive titrations of *Cr*Fdx1–3 resulted in almost identical Nernst fits (Fig. 2 *B*). The results of both titrations were combined before fitting to the one-electron Nernst plots. The semi-log plot analysis yielded $n = 1 \pm 0.1$ for all isoforms validating a poised redox titration.

EPR characterization and midpoint potentials of *Cr*Fdx1 variants

Fig. 1 shows the active site region of *Cr*Fdx1 (45). The highlighted positions S43 and S44 are located in the cluster binding loop region of *Cr*Fdx1 and thus are in proximity to the [2Fe2S] cluster. Whereas S44 is more or less pointing toward the FeS cluster, the hydroxyl group of S43 faces away from it. However, as the loop region of *Cr*Fdx1 is known to be very flexible, which is believed to be important in terms of minimizing the reorganization energy required for rapid electron transfer, the orientation of the side chains at these positions will most likely change in solution. Both primary amides of the protein backbone are situated close enough to one of the bridging cysteine sulfides (3.3 Å) to form a hydrogen bond as part of the NH-S hydrogen bond network unique to plant-type PetF, thus delocalizing the electron density of the cluster (46).

Because of their proximity to and their influence on the FeS cluster, these positions were targeted by site-directed exchange mutagenesis; exchanges to different properties (charge, polarity, size, and hydrophobicity) were implemented for protein variants S43A, S43D, S44D, S44G, and S44R. Subsequently, pulsed Q-band EPR spectra were recorded for all *Cr*Fdx1 variants (Fig. 3). As expected, their rhombic spectra revealed slightly shifted *g*-tensor values in comparison to the wildtype, indicating that the electronic environment of the [2Fe2S] cluster has changed (Table S2). Whereas S44G and S44R exhibit negligible differences in the *g*-tensor values, those of S43A and S44D deviate significantly. Analysis of the EPR spectra did not reveal any correlation between the observed shifts in *g*-values and type and/or position of the mutated amino acids. The detected changes in midpoint potentials of all S44 variants are negligible, whereas S43A and S43D show the highest deviations from the midpoint potential of *Cr*Fdx1 of +80 and −93 mV, respectively (Fig. 3; Table 1). We note that the actual midpoint potential of S43D is possibly even more negative because the midpoint potential of dithionite limited the lowest achievable potential for this variant (37). The potential shift of S43A and S43D goes along with distinct shifts in *g*-values and g_3, respectively (see Fig. 4). For the other variants, no simple correlation between midpoint potential and respective shifts of the *g*-values is observed. Furthermore, S43A presents the highest rhombicity and flexibility among *Cr*Fdx1 variants. In contrast, S43D displays the lowest rhombicity and flexibility.

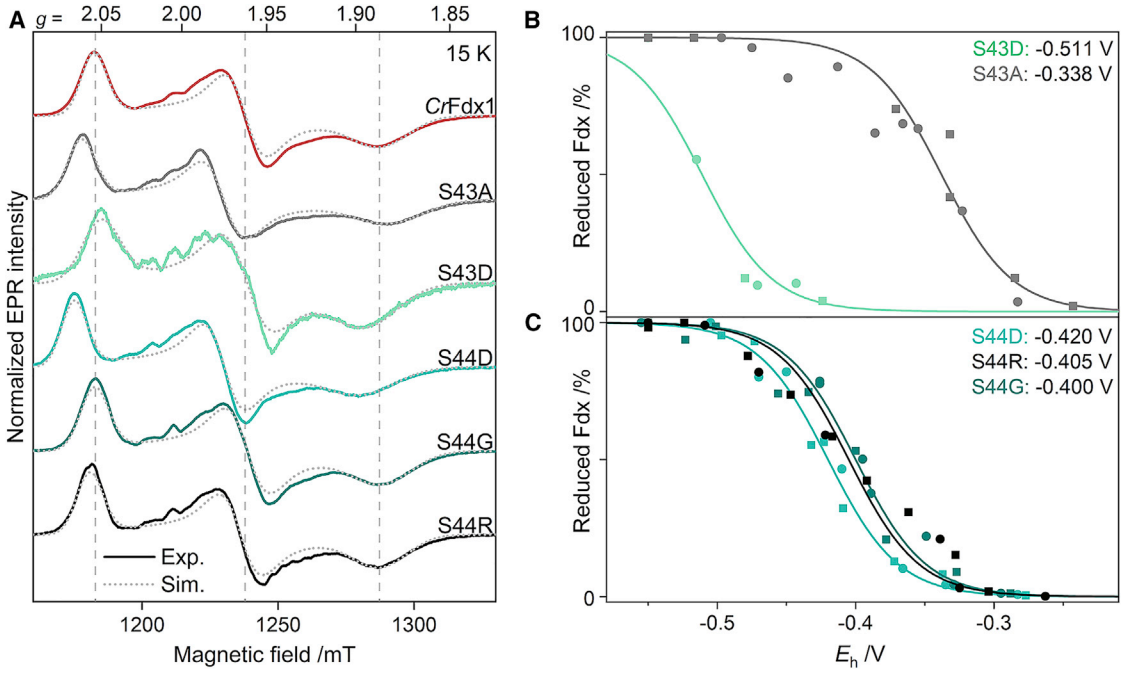

FIGURE 3 (*A*) Comparison of normalized Q-band pseudomodulated pulsed EPR spectra of different *Cr*Fdx1 variants. The samples were reduced with 10 mM NaDT. Simulations are shown with dotted gray traces, and the principal *g*-values of *Cr*Fdx1 are marked with vertical dashed lines. Titration curves of the reductive (*circles*) and oxidative (*squares*) redox potentiometry series of *Cr*Fdx1 variants (*B*) S43 and (*C*) S44 monitored via pulsed EPR spectroscopy at Q-band. The spin concentrations were obtained by double integration of the simulated first-derivative pulsed EPR spectra. The data points were fitted to a one-electron Nernst equation (*solid lines*) yielding the midpoint potential.

DISCUSSION

The precise determination of midpoint potentials is one of the key steps toward understanding the function of a redox protein and its role in complex catalytic reactions. Identifying positions that alter the FeS cluster midpoint potential does not only help to understand the sophisticated and complex influence of the protein environment but also reveals effective parameters for precise manipulation of metalloproteins for biotechnological purposes. It adjusts the metabolic "fate" of the electrons by manipulating the electron carriers (Fdx) as track switches (47,48). In this work, we showed for *Cr*Fdx1 that S43 is an important position close enough to the FeS cluster to alter the electronic structure of the cofactor.

The rhombic EPR line shape of Fdx [2Fe2S] clusters is dominated by *g*-anisotropy. The g_2 and g_3 values are dominated by the strong anisotropy of the Fe^{2+} ion, whereas the low-field value, g_1, is determined by the Fe^{3+} ion (41,49,50). Therefore, shifts in *g*-values suggest structural and/or electrostatic changes within and/or in the vicinity of the active center (41–43). Despite the observed small variations, the *g*-values and also the rhombicity parameter, η, of all Fdx isoforms and variants detected in this work fall into the characteristic average Fe^{3+}-Fe^{2+}-S-C dihedral angle range described by Gambarelli and Mouesca (42) for plant-type Fdxs. These results indicate that the structure around the [2Fe2S] clusters of Fdxs does not change dramatically upon site-directed exchange mutagenesis. This is not always self-evident as shown for the [2Fe2S] cluster of HydC from *Thermotoga maritima* (11). Furthermore, the similar g_{iso} values indicate the absence of strong shifts in the spin localization degree of the [2Fe2S] cluster. A comparison of the physical differences listed in Table S2 and detected E_ms did not establish a correlation among the Fdx isoforms. However, strikingly, for the *Cr*Fdx1 variants S43A and S43D, a possible relation is observed (see Fig. 4).

The origin of the difference in midpoint potentials of *Cr*Fdx1 and *Cr*Fdx2 is not fully understood yet. Structural differences in the vicinity of their [2Fe2S] clusters were suggested to be one of the underlying reasons (26). Primary ligands determine the overall redox potential range of a given metal center. However, interactions with the secondary coordination sphere have been shown to fine-tune the potential of metal cofactors within redox proteins. The midpoint potential of *Cr*Fdx2 was lowered to a value comparable to that of *Cr*Fdx1 by employing the substitution M62F (26). In wildtype *Cr*Fdx1, as observed in many other FeS proteins, the backbone nitrogen atoms in the cluster binding loop area form NH-S hydrogen bonds with the cysteine sulfur atoms and the sulfur atoms of the [2Fe2S] cluster. The backbone amide of S43 is also

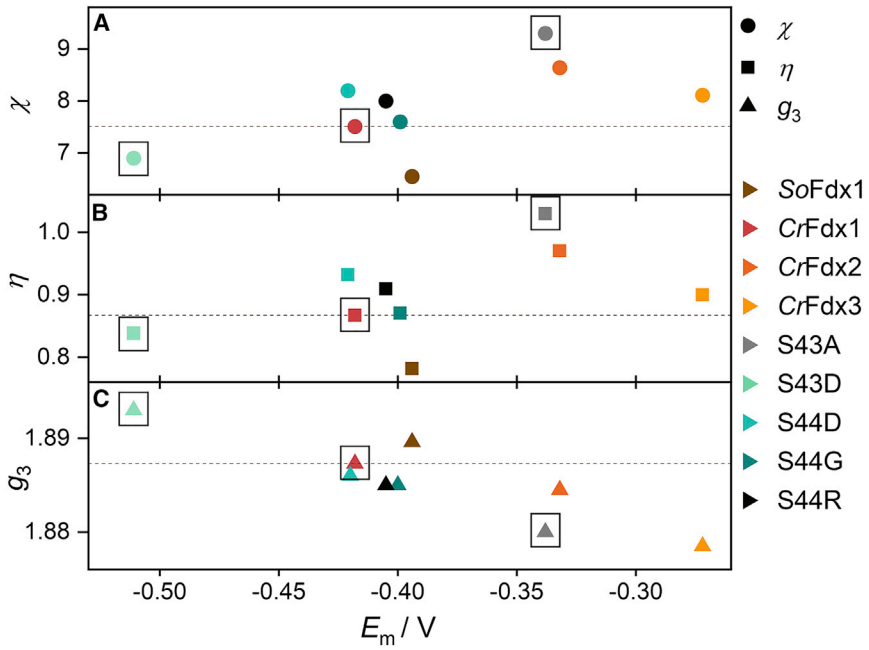

FIGURE 4 Correlation between the midpoint potentials, E_m, of the Fdx isoforms and variants and parameters (*A*) χ, (*B*) the rhombicity η, and (*C*) the g_3 component. *Cr*Fdx1 and its variants that resulted in significant midpoint potential shifts are marked with squares. The dashed lines show the χ-, η-, and g_3 values of *Cr*Fdx1.

involved in a hydrogen bond toward the μ-sulfide atom of the FeS cluster. Thus, the impact of exchanges at this position might be caused by a weakening or disruption of that bond because of steric changes in the protein loop. This is underlined by the detected physical differences, such as χ, η, and the *g*-values, suggesting structural/electrostatic changes nearby and/or within the redox cluster. Among *Cr*Fdx1 variants, S43A, the variant with substantial *g*-shifts and the highest χ- and η-values, displays the highest E_m, whereas the one with the lowest E_m, S43D, shows the lowest χ- and η-values. Interestingly, the g_1 and g_2 values of S43D are highly similar to the ones measured for *Cr*Fdx1, but its g_3 value is distinct. A slight correlation is observed when g_3 values are plotted against detected E_ms (see Fig. 4). Such a relationship has not been reported so far; however, these findings need to be interpreted with care as our data is restricted to a small number of Fdxs investigated in this work. Our results furthermore suggest that the flexibility of the cluster is related to the midpoint potential, as seen in Fig. 4 for S43 variants (χ versus E_m). In *Anabaena* 7120 Fdx1, S47 (corresponding to S43 in *C. reinhardtii*) is prone to structural changes upon reduction of the FeS cluster (51–53). Therefore, this position might be crucial to buffer structural changes in the protein environment, for example by redox transitions. Increasing or restricting the flexibility at this position might therefore in turn have a higher impact on the electronic features and solvent accessibility of the adjacent FeS cluster. The correlation observed between the E_ms of the *Cr*Fdx1 S43 variants and η, which associate with variations of average Fe^{3+}-Fe^{2+}-S-C dihedral angles, further supports the important role of the small structural changes in affecting the redox potentials (54). Yet, further research, including different *Cr*Fdx isoforms and variants along with theoretical calculations, are needed to reveal the significance of the observed relationships.

Apart from the impact of hydrogen bonds, the introduction of net charge was shown to have drastic effects on the midpoint potential (10). We showed that the introduction of a negative charge (S43D) decreased the midpoint potential, whereas exchanging the negative dipole with a noncharged amino acid (S43A) led to a more positive net charge and therefore to a more positive potential. Exchanges of S44 barely changed the midpoint potential. Furthermore, the physical differences between the variants of residue S44 were negligible (Table S2). As S44 shares many attributes with S43 (amide H-bond and proximity to the FeS cluster), this underlines the complex nature of the protein framework and its influence on the bound cofactor. It can be noted that in wildtype *Cr*Fdx1, S44 is H-bonded to S36. Exchanges of S44 might therefore lead to a disruption of this H-bond, which could result in a reorientation of both side chains and associated regions and thus a composition of different effects on the FeS cluster.

Last, we note that although cw EPR spectroscopy at X-band frequencies has been established as a powerful tool for obtaining midpoint potentials, pulsed EPR is beneficial when there exist multiple species with distinct relaxation times. Then, relaxation filtering can be used to separate and/or suppress their signals (see the mediator mix signal marked with an asterisk in Fig. S3 *A* vs. Fig. S3 *B*). This approach can additionally be applied at even higher microwave frequencies when low *g*-anisotropy

TABLE 1 Midpoint potentials, $E_{m,7.5}$, obtained at pH = 7.5 of all Fdxs investigated in this work

Ferredoxin	$E_{m,7.5}$/mV
*So*Fdx	−394 ± 5/7
*Cr*Fdx1	−419 ± 5
*Cr*Fdx2	−332 ± 5
*Cr*Fdx3	−272 ± 4
*Cr*Fdx1 S43A	−338 ± 9
*Cr*Fdx1 S43D	−511 ± 17
*Cr*Fdx1 S44D	−420 ± 4
*Cr*Fdx1 S44G	−400 ± 8
*Cr*Fdx1 S44R	−405 ± 9

See Materials and methods for details of the given error margin.

or multiple species with similar *g*-factors need to be resolved. Furthermore, the required sample volume decreases substantially at higher frequencies (∼150 μL at 9.5 GHz vs. 5–10 μL at 34 GHz vs. 0.5 μL at 94 GHz). Therefore, our pulsed EPR-monitored redox potentiometry technique at Q-band presents an alternative method that overcomes the limitations of the X-band cw EPR technique for certain systems.

CONCLUSIONS

In this study, we determined the midpoint potential of *Cr*Fdx3 for the first time, to our knowledge, using pulsed EPR at Q-band. *Cr*Fdx3 might be a potential target for manipulating catalysis in *C. reinhardtii* as it was suggested to have interactions with [FeFe]-hydrogenases HydA1 and HydA2 in this organism. Furthermore, we showed that single point mutations in the vicinity of the [2Fe2S] cluster of *Cr*Fdx1 tune the midpoint potential in the range of −338 to −511 mV. We identified S43 as an optimal target for manipulating the midpoint potential by introducing or removing the net charge. Our results serve as a basis to design new experiments for unraveling the distinct functions of Fdx isoforms and illuminate the decisive role of individual positions in the secondary ligand sphere of the cofactor in tuning the midpoint potential of redox proteins.

SUPPORTING MATERIAL

Supporting material can be found online at https://doi.org/10.1016/j.bpr.2021.100016.

AUTHOR CONTRIBUTIONS

M.H. performed research, analyzed data, and partially wrote the manuscript. A.G. performed research, analyzed data, and partially wrote the manuscript. D.B. and Y.K. contributed to some of the data acquisition Y.K. and VE helped writing the manuscript. M.W. designed research and helped writing the manuscript. T.H. and M.K. designed and funded research, partially analyzed data, and wrote the manuscript.

ACKNOWLEDGMENTS

We thank Dr. Alexander Schnegg (Max Planck Institute for Chemical Energy Conversion) for providing access to his X-band EPR spectrometer. We thank Dr. Edward Reijerse for helpful discussions.

This work is funded by the Deutsche Forschungsgemeinschaft (German Research Foundation) under Germany's Excellence Strategy (EXC 2033 - 390677874 – RESOLV). T.H. acknowledges finance from the Deutsche Forschungsgemeinschaft (Priority Programme SPP1927 `FeS for Life' and HA 2555/10-1).

DECLARATION OF INTERESTS

The authors declare no competing interests.

REFERENCES

1. Beinert, H. 2000. Iron-sulfur proteins: ancient structures, still full of surprises. *J. Biol. Inorg. Chem.* 5:2–15.
2. Lill, R. 2009. Function and biogenesis of iron-sulphur proteins. *Nature.* 460:831–838.
3. Liu, J., S. Chakraborty, …, Y. Lu. 2014. Metalloproteins containing cytochrome, iron-sulfur, or copper redox centers. *Chem. Rev.* 114:4366–4469.
4. Page, C. C., C. C. Moser, and P. L. Dutton. 2003. Mechanism for electron transfer within and between proteins. *Curr. Opin. Chem. Biol.* 7:551–556.
5. Jin, Q., and C. M. Bethke. 2002. Kinetics of electron transfer through the respiratory chain. *Biophys. J.* 83:1797–1808.
6. Cammack, R., K. K. Rao, …, L. J. Rogers. 1977. Midpoint redox potentials of plant and algal ferredoxins. *Biochem. J.* 168:205–209.
7. Zuris, J. A., D. A. Halim, …, P. A. Jennings. 2010. Engineering the redox potential over a wide range within a new class of FeS proteins. *J. Am. Chem. Soc.* 132:13120–13122.
8. Bak, D. W., and S. J. Elliott. 2014. Alternative FeS cluster ligands: tuning redox potentials and chemistry. *Curr. Opin. Chem. Biol.* 19:50–58.
9. Hosseinzadeh, P., N. M. Marshall, …, Y. Lu. 2016. Design of a single protein that spans the entire 2-V range of physiological redox potentials. *Proc. Natl. Acad. Sci. USA.* 113:262–267.
10. Hosseinzadeh, P., and Y. Lu. 2016. Design and fine-tuning redox potentials of metalloproteins involved in electron transfer in bioenergetics. *Biochim. Biophys. Acta.* 1857:557–581.
11. Birrell, J. A., C. Laurich, …, W. Lubitz. 2016. Importance of hydrogen bonding in fine tuning the [2Fe-2S] cluster redox potential of HydC from Thermotoga maritima. *Biochemistry.* 55:4344–4355.
12. Li, B., P. Steindel, …, S. J. Elliott. 2021. Maximizing (electro)catalytic CO_2 reduction with a ferredoxin-based reduction potential gradient. *ACS Catal.* 11:4009–4023.
13. Mutter, A. C., A. M. Tyryshkin, …, P. G. Falkowski. 2019. De novo design of symmetric ferredoxins that shuttle electrons in vivo. *Proc. Natl. Acad. Sci. USA.* 116:14557–14562.
14. Cammack, R., D. S. Patil, and V. M. Fernandez. 1985. Electron-spin-resonance/electron-paramagnetic-resonance spectroscopy of iron-sulphur enzymes. *Biochem. Soc. Trans.* 13:572–578.
15. Zanello, P. 2014. The competition between chemistry and biology in assembling iron–sulfur derivatives. Molecular structures and electrochemistry. Part II. {[Fe2S2](SγCys)4} proteins. *Coord. Chem. Rev.* 280:54–83.
16. Sands, R. H., and W. R. Dunham. 1974. Spectroscopic studies on two-iron ferredoxins. *Q. Rev. Biophys.* 7:443–504.

17. Beinert, H., R. H. Holm, and E. Münck. 1997. Iron-sulfur clusters: nature's modular, multipurpose structures. *Science.* 277:653–659.
18. Yang, W., T. M. Wittkopp, …, A. R. Grossman. 2015. Critical role of Chlamydomonas reinhardtii ferredoxin-5 in maintaining membrane structure and dark metabolism. *Proc. Natl. Acad. Sci. USA.* 112:14978–14983.
19. Sawyer, A., and M. Winkler. 2017. Evolution of Chlamydomonas reinhardtii ferredoxins and their interactions with [FeFe]-hydrogenases. *Photosynth. Res.* 134:307–316.
20. Bertini, I., C. Luchinat, …, P. R. Vasos. 2002. Browsing gene banks for Fe2S2 ferredoxins and structural modeling of 88 plant-type sequences: an analysis of fold and function. *Proteins.* 46:110–127.
21. Schmitter, J. M., J. P. Jacquot, …, P. Decottignies. 1988. Purification, properties and complete amino acid sequence of the ferredoxin from a green alga, Chlamydomonas reinhardtii. *Eur. J. Biochem.* 172:405–412.
22. Galvan, F., A. Marquez, and E. Fernandez. 1985. Physicochemical properties of ferredoxin from Chlamydomonas reinhardii. *Z. Naturforsch. C.* 40c:373–378.
23. Happe, T., and J. D. Naber. 1993. Isolation, characterization and N-terminal amino acid sequence of hydrogenase from the green alga Chlamydomonas reinhardtii. *Eur. J. Biochem.* 214:475–481.
24. Peden, E. A., M. Boehm, …, A. Dubini. 2013. Identification of global ferredoxin interaction networks in Chlamydomonas reinhardtii. *J. Biol. Chem.* 288:35192–35209.
25. Terauchi, A. M., S.-F. Lu, …, S. S. Merchant. 2009. Pattern of expression and substrate specificity of chloroplast ferredoxins from Chlamydomonas reinhardtii. *J. Biol. Chem.* 284:25867–25878.
26. Boehm, M., M. Alahuhta, …, A. Dubini. 2016. Crystal structure and biochemical characterization of Chlamydomonas FDX2 reveal two residues that, when mutated, partially confer FDX2 the redox potential and catalytic properties of FDX1. *Photosynth. Res.* 128:45–57.
27. Martínez-Espinosa, R. M., D. J. Richardson, …, M. J. Bonete. 2007. Spectopotentiometric properties and salt-dependent thermotolerance of a [2Fe-2S] ferredoxin-involved nitrate assimilation in Haloferax mediterranei. *FEMS Microbiol. Lett.* 277:50–55.
28. Hagedoorn, P.-L., L. van der Weel, and W. R. Hagen. 2014. EPR monitored redox titration of the cofactors of *Saccharomyces cerevisiae* Nar1. *J. Vis. Exp* e51611.
29. Wright, J. J., E. Salvadori, …, M. M. Roessler. 2016. Small-volume potentiometric titrations: EPR investigations of Fe-S cluster N2 in mitochondrial complex I. *J. Inorg. Biochem.* 162:201–206.
30. Dutton, P. L. 1978. Redox potentiometry: determination of midpoint potentials of oxidation-reduction components of biological electron-transfer systems. *Methods Enzymol.* 54:411–435.
31. Vogel, H. J., and D. M. Bonner. 1956. Acetylornithinase of *Escherichia coli*: partial purification and some properties. *J. Biol. Chem.* 218:97–106.
32. Palma, P. N., B. Lagoutte, …, F. Guerlesquin. 2005. Synechocystis ferredoxin/ferredoxin-NADP(+)-reductase/NADP+ complex: structural model obtained by NMR-restrained docking. *FEBS Lett.* 579:4585–4590.
33. Nordstrom, D. K., and F. D. Wilde. 2005. Chapter 6.5. Reduction-oxidation potential (electrode method). *In* U.S. Geological Survey Techniques of Water-Resources Investigations, Book 9: Handbooks for Water-Resources Investigations. F. D. Wilde and D. B. Radtke, eds. U.S. Geological Survey.
34. Aliverti, A., W. R. Hagen, and G. Zanetti. 1995. Direct electrochemistry and EPR spectroscopy of spinach ferredoxin mutants with modified electron transfer properties. *FEBS Lett.* 368:220–224.
35. Stoll, S., and A. Schweiger. 2006. EasySpin, a comprehensive software package for spectral simulation and analysis in EPR. *J. Magn. Reson.* 178:42–55.
36. Aasa, R., and T. Vänngård. 1975. EPR signal intensity and powder shapes: a reexamination. *J. Magn. Reson.* 19:308–315.
37. Mayhew, S. G. 1978. The redox potential of dithionite and SO-2 from equilibrium reactions with flavodoxins, methyl viologen and hydrogen plus hydrogenase. *Eur. J. Biochem.* 85:535–547.
38. Hagen, W. R. 2014. Biomolecular EPR Spectroscopy. CRC Press, Boca Raton, FL.
39. Stombaugh, N. A., J. E. Sundquist, …, W. H. Orme-Johnson. 1976. Oxidation-reduction properties of several low potential iron-sulfur proteins and of methylviologen. *Biochemistry.* 15:2633–2641.
40. Roncaroli, F., E. Bill, …, M.-E. Pandelia. 2015. Cofactor composition and function of a H_2-sensing regulatory hydrogenase as revealed by Mössbauer and EPR spectroscopy. *Chem. Sci. (Camb.).* 6:4495–4507.
41. Bertrand, P., and J. P. Gayda. 1979. A theoretical interpretation of the variations of some physical parameters within the [2Fe-2S] ferredoxin group. *Biochim. Biophys. Acta.* 579:107–121.
42. Gambarelli, S., and J.-M. Mouesca. 2004. Correlation between the magnetic g tensors and the local cysteine geometries for a series of reduced [2Fe-2S*] protein clusters. A quantum chemical density functional theory and structural analysis. *Inorg. Chem.* 43:1441–1451.
43. Orio, M., and J.-M. Mouesca. 2008. Variation of average g values and effective exchange coupling constants among [2Fe-2S] clusters: a density functional theory study of the impact of localization (trapping forces) versus delocalization (double-exchange) as competing factors. *Inorg. Chem.* 47:5394–5416.
44. Schorsch, M., M. Kramer, …, G. T. Hanke. 2018. A unique ferredoxin acts as a player in the low-iron response of photosynthetic organisms. *Proc. Natl. Acad. Sci. USA.* 115:E12111–E12120.
45. Ohnishi, Y., N. Muraki, …, G. Kurisu. 2020. X-ray dose-dependent structural changes of the [2Fe-2S] ferredoxin from Chlamydomonas reinhardtii. *J. Biochem.* 167:549–555.
46. Fukuyama, K. 2004. Structure and function of plant-type ferredoxins. *Photosynth. Res.* 81:289–301.
47. Rumpel, S., J. F. Siebel, …, M. Winkler. 2014. Enhancing hydrogen production of microalgae by redirecting electrons from photosystem I to hydrogenase. *Energy Environ. Sci.* 7:3296–3301.
48. Wiegand, K., M. Winkler, …, M. Rögner. 2018. Rational redesign of the ferredoxin-$NADP^+$-oxido-reductase/ferredoxin-interaction for photosynthesis-dependent H_2-production. *Biochim. Biophys. Acta Bioenerg.* 1859:253–262.
49. Gibson, J. F., D. O. Hall, …, F. R. Whatley. 1966. The iron complex in spinach ferredoxin. *Proc. Natl. Acad. Sci. USA.* 56:987–990.
50. Hearshen, D. O., W. R. Hagen, …, W. R. Dunham. 1986. An analysis of g strain in the EPR of two [2Fe2S] ferredoxins. Evidence for a protein rigidity model. *J. Magn. Reson.* 69:440–459.
51. Dugad, L. B., G. N. La Mar, …, I. Bertini. 1990. Identification of localized redox states in plant-type two-iron ferredoxins using the nuclear Overhauser effect. *Biochemistry.* 29:2263–2271.
52. Morales, R., M. H. Charon, …, M. Frey. 1999. Refined X-ray structures of the oxidized, at 1.3 A, and reduced, at 1.17 A, [2Fe-2S] ferredoxin from the cyanobacterium Anabaena PCC7119 show redox-linked conformational changes. *Biochemistry.* 38:15764–15773.
53. Morales, R., M. H. Charon, …, M. Frey. 2000. A redox-dependent interaction between two electron-transfer partners involved in photosynthesis. *EMBO Rep.* 1:271–276.
54. Ergenekan, C. E., D. Thomas, …, T. Ichiye. 2003. Prediction of reduction potential changes in rubredoxin: a molecular mechanics approach. *Biophys. J.* 85:2818–2829.